PAPER

Enhancement of electrochromic properties using nanostructured amorphous tungsten trioxide thin films†

Cheong-Ha Kim,[ab] Yu-Sung Kim,[a] Jin-Young Choi,[a] In-Sik Lee,[a] Byung-Chul Cha,[a] Dae-Wook Kim [ID] *[a] and Jewon Lee*[b]

Electrochromic technologies have recently attracted attention due to their energy-saving performance for reducing green gas emissions. The materials design and preparation of electrochromic materials with sufficient microstructure and crystallographic features for suitable ion intercalation/deintercalation are essential for high performance and efficiency. In the present work, nanostructured amorphous tungsten trioxide (WO_3) films are electrodeposited to enhance electrochromic properties by controlling the pH of electrolytes. Electron microscopy and spectroelectrochemical analysis demonstrate that smaller grain sizes result in larger electrochemical reactive surface areas and shorter ion diffusion lengths. Consequently, the ions efficiently intercalated and deintercalated during the coloring and bleaching states, respectively. In particular, prepared WO_3 films at electrolyte pH 1.4 demonstrate high optical modulation (74.83%) and good transmittance switching speeds (1.56 and 2.06 s during coloring and bleaching, respectively) at 650 nm, as well as comparable coloration efficiency (61.92 cm^2 C^{-1} at 650 nm).

Introduction

Greenhouse gas emissions are the main cause of global warming, and are expected to worsen. According to the International Energy Agency (IEA) report, the carbon dioxide emissions and energy consumption of the global building sector are 36% and 39%, respectively.[1,2] Thus, an enhancement in energy efficiency in buildings is necessary to reduce carbon dioxide emissions.

Electrochromic smart windows have recently attracted attention because of their energy-saving performance, such as solar radiation.[3,4] A fundamental of the electrochromic technology is as follows; when voltages are applied to a device, Li^+ or H^+ ions in the electrolyte migrate to the functional film, and their intercalation and deintercalation processes lead to changes in optical properties, including coloration and transmittance.[5–7]

Functional film materials can be classified into two types based on their reaction mechanism: anodic (V_2O_5, NiO, Co_3O_4, etc.) and cathodic (WO_3, TiO_2, Nb_2O_5, etc.) coloration materials.[8–15] Among these materials, WO_3 has been widely researched as a coloration material in electrochromic devices

because of its good coloration efficiency, cycle reversibility, lifetime, and chemical stability.[16,17]

WO_3 has an empty-perovskite structure composed of corner-sharing WO_6 octahedra. A cation is available to insert into the interstitial sites, and when a negative potential is applied, a cation is intercalated, which leads to a coloration. However, when a positive potential is applied, an intercalated cation is deintercalated from the interstitial site, leading to bleaching.[16,18] These electrochromic reactions can be described as follows.

$$WO_3 \text{ (colorless)} + xe^- + xM^+ \rightarrow M_xWO_3 \text{ (dark blue)}$$
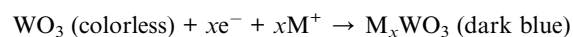
where M is the intercalated ions and x is concentration of the ions.

Coloration is possible with both amorphous and crystalline WO_3, and their reactions are caused by tiny polaron hopping and the Drude model, respectively.[19,20] Because of the facile migration of cations in amorphous WO_3, it outperforms crystalline WO_3 in terms of quick reaction and increased efficiency.[20] Moreover, since nanostructured WO_3 provide large surface area with shorten ions diffusion length, which could achieve faster intercalation/deintercalation reaction and switching than that of bulk structure.[21,22]

Meanwhile, there are many methods for preparing WO_3 films, such as electrodeposition, laser deposition, spray pyrolysis, thermal evaporation, magnetron sputtering, and hydrothermal methods.[7,23–27] Among these, electrodeposition used in this study is widely used for preparing WO_3 because of several

[a]Advanced Manufacturing Process R&D Group, Ulsan Regional Division, Korea Institute of Industrial Technology (KITECH), 55, Jongga-ro, Jung-gu, Ulsan, 44313, Korea. E-mail: dwkim@kitech.re.kr

[b]Department of Nanoscience and Engineering, Inje University, Gimhae, Gyeongnam, 50834, Korea. E-mail: jwlee@inje.ac.kr

† Electronic supplementary information (ESI) available. See DOI: https://doi.org/10.1039/d2ra06472c

merits, such as a simple process under room temperature and atmospheric pressure, the possibility of large-area deposition, and low capital cost.[28,29]

In this study, WO_3 films are prepared using electrodeposition for coloration materials, and the electrolyte pH in the bath is controlled by adding perchloric acid ($HClO_4$). Because the variation of electrolyte pH is expected to facilitate controlling film structure. The changes of electrolyte pH imply to control amount of reactant with tungstate species, which can induce variety of nucleation density. As a result, the controlled parameter would affect to structural properties including grain size and film density.

The influence of controlled pH during electrodeposition on nucleation density and their correlation with coloration efficiency is investigated. The most challenging issue in this study is investigating the effect of nucleation density on the electrochromic properties with the reaction speed and efficiency.

Experimental

A fluorine-doped tin oxide (FTO)-coated glass ($7 \leq \Omega$ sq^{-1}) substrates were cut into 0.8×3 cm^2 pieces and then cleaned with isopropyl alcohol, acetone, and ultrapure water for 20 min. After washing, the FTO glass was air dried. The electrodeposition bath solution was synthesized by mixing 0.515 g sodium tungstate dihydrate ($Na_2WO_4 \cdot 2H_2O$) with 125 ml ultrapure water (25 ± 2 °C) and stirring the solution for 30 min. After that, 0.325 ml hydrogen peroxide (H_2O_2) was added to the solution, and the hydrogen ion concentration (pH) in the bath solution was adjusted between pH 1.8 and 1.2 by adding varying concentrations of $HClO_4$. Additional stirring was performed for 30 min, and then the solution was used as an electrodeposition bath solution. WO_3 thin film was prepared using a three-electrode potentiostat/galvanostat (PL-9, Physio Lab) equipment in an electrochemical setup where FTO glass, platinum coil, and Ag/AgCl (sat. 3 M KCl) electrodes were used as working, counter, and reference electrodes, respectively. An area of 0.8×1.5 cm^2 working electrode was immersed in the bath solution. During the electrodeposition, the bath solution was stirred at 80 rpm, and a constant potential of −630 mV was applied to the working electrode for 360 s. The deposited WO_3 film was washed with ultrapure water and dried at room temperature for 24 h for stabilization. The deposited WO_3 films at pHs 1.8, 1.6, 1.4, and 1.2 were denoted as $pH1.8WO_3$, $pH1.6WO_3$, $pH1.4WO_3$, and $pH1.2WO_3$, respectively. The crystal structure of the WO_3 films was analyzed using X-ray diffraction (XRD, Ultimate IV, Rigaku) with a Cu Kα source ($\lambda = 1.5418$ Å) at 2-theta ranging from 20° to 60° with 0.02° step size. The surface morphology, film thickness, and energy dispersive X-ray spectroscopy (EDS) of the WO_3 films were measured using a field emission scanning electron microscope (FE-SEM, SU8020, HITACH). An additional surface property was investigated using atomic force microscopy (AFM, XE-100, Park Systems). The electrochemical properties of WO_3 films were determined using a three-electrode electrochemical cell with WO_3–FTO glass, platinum coil, and Ag/AgCl (sat. 3 M KCl) as working, counter, and reference electrodes, respectively. The electrodes were

immersed in 1.0 M lithium perchlorate ($LiClO_4$, Wako, $\geq$98%) and propylene carbonate (PC, JUNSEI, 98%) electrolyte. The cyclic voltammetry (CV) was measured for two cycles by applying a potential range of −1.0 to +1.0 V at a sweep rate of 50 mV s^{-1}, while the chronoamperometry (CA) was measured by applying the same potential range for 15 s. During chronoamperometry measurement, the optical properties at 650 nm wavelength were measured *in situ* using a UV-Visible spectrophotometer (UV-Vis, Evolution 220, Thermo).

Results and discussion

Preparation of WO_3 films

The WO_3 films were deposited using the following reactions during the electrodeposition, which was conducted at constant voltages, stirring rate, and time.[30]

$$2WO_4^{2-} + 4H_2O_2 \rightarrow W_2O_{11}^{2-} + 2OH^- + 3H_2O$$

$$W_2O_{11}^{2-} + (2+3x)H^+ + 3xe^- \rightarrow 2H_xWO_3 + \frac{(2+x)}{2}H_2O$$
$$+ \frac{(8-x)}{4}O_2,$$

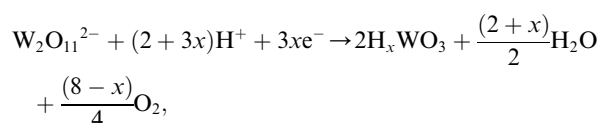$$H_xWO_3 \rightarrow WO_3 + xH^+ + xe^-$$

Fig. 1a shows the variation of current density at different pHs of 1.2–1.8 during electrodeposition. The current density tended to increase as the pH decreased. Because the hydrogen ions (H^+) that react with peroxytungstate ($W_2O_{11}^{2-}$) in the lower pH conditions increase, nucleation density might be increased; thereby, more tungsten bronze (H_xWO_3) is formed, *i.e.*, decreased electrolyte pH leads to increase nucleation density, resulting in increased current density during electrodeposition. Fig. 1b shows the deposition rate depending on the variation of electrolyte pH. Due to the increased nucleation rate, the thickness of deposited WO_3 increases with increasing current density (inset of Fig. 3).

Characterization

XRD patterns were conducted to examine the crystallinity of the electrodeposited films (Fig. 2). All the films show FTO peaks, and there are no obvious peaks corresponding to WO_3. The $pH1.2WO_3$ film was post-annealed at 400 °C to obtain structural information, and then it was compared to others. The post-annealed $pH1.2WO_3$ film showed (002), (020), and (200) peaks of monoclinic tungsten oxide in the XRD patterns,[31] implying that all films are formed as amorphous phases. Additionally, the obtained EDS spectra (Fig. S1†) confirmed that the impurities are not formed in the WO_3 films. As a result, the nanostructured amorphous WO_3 films are successfully prepared.

Based on the above section, an increasing current density is related to the nucleation rate,[32] which highly affects the grain size of WO_3. As shown in the FE-SEM images (Fig. 3), the grain
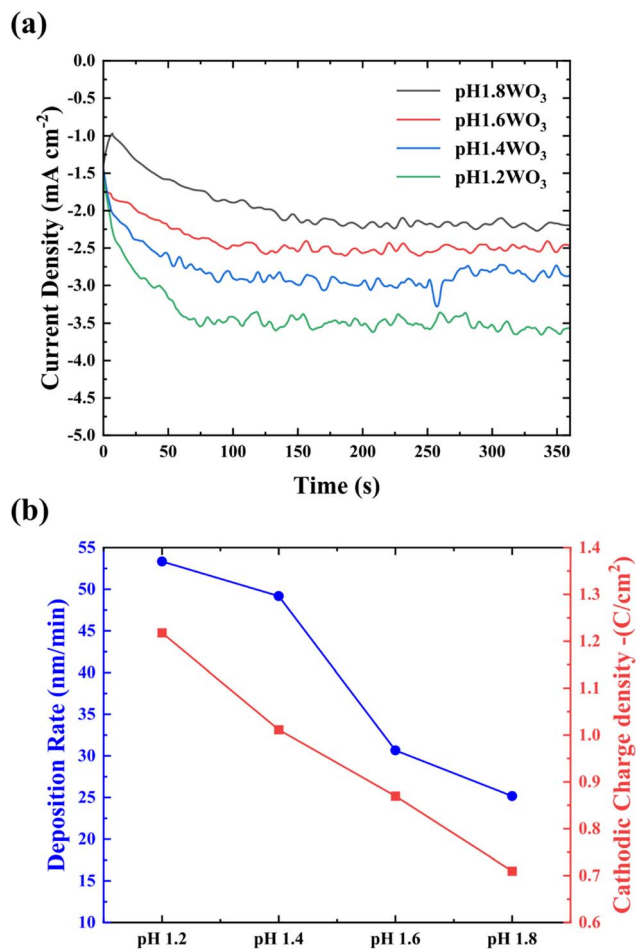
Fig. 1 (a) Current density of WO$_3$ deposited at various pH bath levels. (b) Variation of deposition rate (nm/min) with bath pH conditions and cathodic charge density.
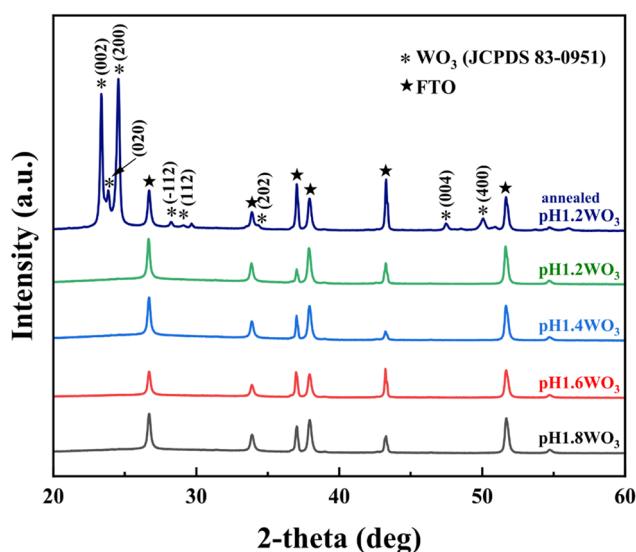

Fig. 2 XRD patterns of the WO$_3$ thin films prepared at various electrolytes pH.

size tends to increase as the electrolyte pH increases. The pH1.2WO$_3$ film particularly presented a relatively small grain size and high density. However, such a denser structure could reduce the porosity of films, which might negatively contribute to cation intercalation/deintercalation.

Further investigation of the morphology was examined using AFM. In Fig. 4, the roughness (R_{ms}) linearly decreased with a decrease in pH. These results were consistent with the FE-SEM observations, which showed that a controlled electrolyte pH during electrodeposition could effectively control grain size.

From the obtained results, the lower electrolyte pH induces small grain size and densified film, *i.e.*, the specific surface area was increased, and the porosity was decreased. Therefore, the effect of these phenomena on the electrochromic properties will be discussed in the electrochemical analysis.

Electrochemistry and spectroelectrochemistry

To examine the morphological effect, the CV with the 1.0 M LiClO$_4$ and PC electrolyte was conducted in the range of −1.0 to +1.0 V (*vs.* Ag/AgCl). In Fig. 5, the area of CV curves is related to the charge storage capacity, which might be attributed to the specific surface area and film thickness.[33,34] Furthermore, the diffusion coefficient of Li$^+$ was calculated using Randles–Sevick's equation.[35]

$$i_p = 2.72 \times 10^5 \times n^{\frac{3}{2}} \times D^{\frac{1}{2}} \times C \times \nu^{\frac{1}{2}}, \tag{1}$$

where D is the diffusion coefficient, i_p is the cathodic peak current density, n is the number of electrons (Li$^+$ = 1), C is the concentration of ions (1 mol cm^{-3}), and ν is the sweep rate.

Table 1 summarizes the kinetic parameters. As predicted, the calculated D presented a tendency to enhance with small grain size, which might originate from the large electrochemical reactive surface areas (ERSA) and shortened Li$^+$ diffusion lengths.[6,36] However, small degradation in the pH1.2WO$_3$ might be related to an excessively small grain size, which could create numerous interfaces, thereby increasing interfacial resistance.[37]

CA was conducted using 1.0 M LiClO$_4$ with PC electrolyte at 1.0 and −1.0 voltages to evaluate electrochromic performance with the reactivity for ion insertion/extraction. Additionally, UV-Visible spectroscopy (UV-Vis) was used to investigate the velocity of switching between coloring and bleaching (Fig. 6). Fig. S2† shows the transmittance spectra in bleaching and coloration state at wavelength from 300 to 900 nm. The transmittance modulation of WO$_3$ films tended to increase with decreasing electrolyte pH in both visible and near-infrared region.

The charge density (Q) during electrochromic was calculated from the spectra in Fig. 6a using the following equation.[38]

$$Q = \int i \mathrm{d}t \tag{2}$$

The WO$_3$ films exhibited charge densities of 13.99, 20.97, 33.36, and 31.25 mC cm^{-2} in decreasing order of electrolyte pH. This increasing charge density with decreasing pH trends could be attributed to a relatively large specific surface area and
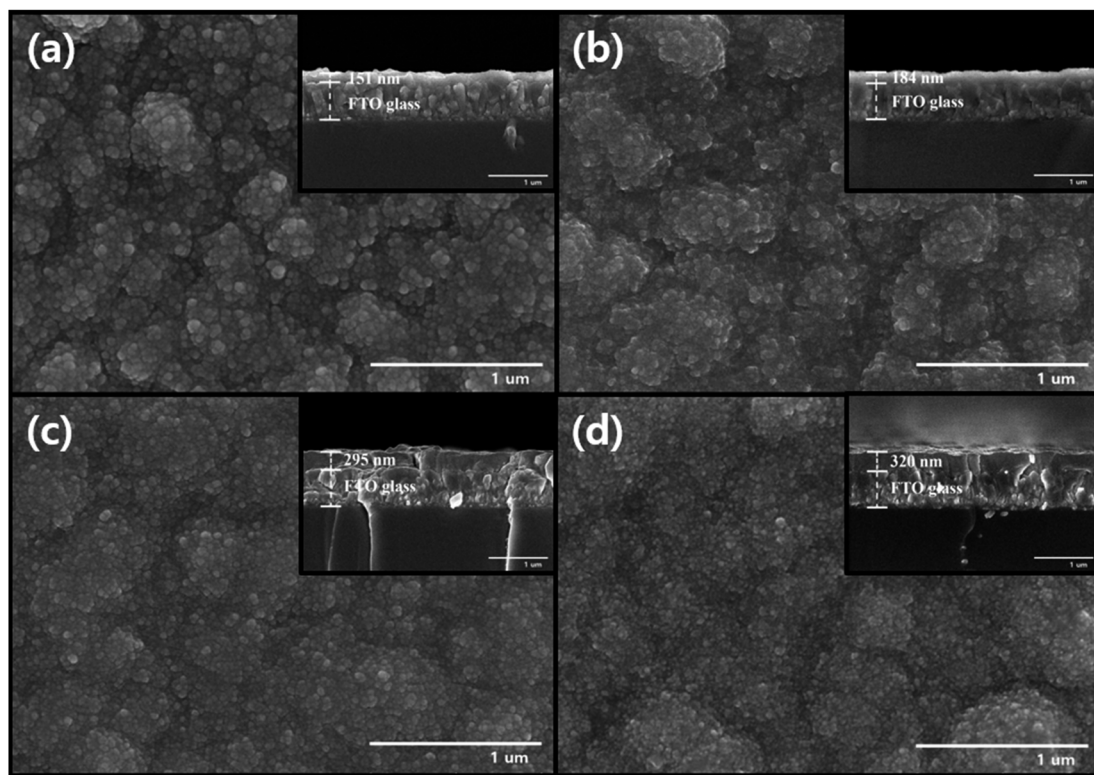
Paper

Fig. 3 FE-SEM images for surface and cross-section (inset) of the (a) pH1.8WO$_3$, (b) pH1.6WO$_3$, (c) pH1.4WO$_3$, and (d) pH1.2WO$_3$.
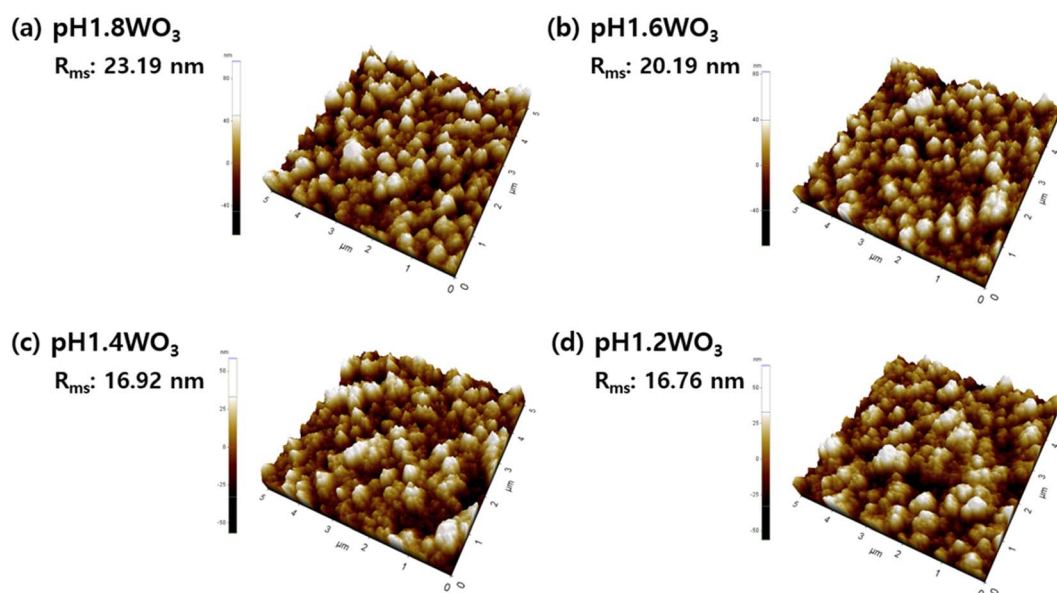

Fig. 4 Three-dimensional AFM images of WO$_3$ thin films prepared at (a) pH 1.8, (b) pH 1.6, (c) pH1.4, and (d) pH 1.2.

thicker film thickness with increasing active mass.[36,39] The slightly lower charge density for pH1.2WO$_3$ is because the film's interior is densified, and the multiple interfaces may disrupt ion intercalation.[40,41]

Table 2 summarizes the obtained spectroelectrochemical parameters. All films presented sharp spectra during transmittance switching (Fig. 6b), showing a rapid switching time of around 2 s (Table 2). This rapid reaction could be because of the amorphous nanostructure, which could provide large reactive areas with fast ion migration. Additionally, higher charge density at the coloration state results in improved transmittance modulation.
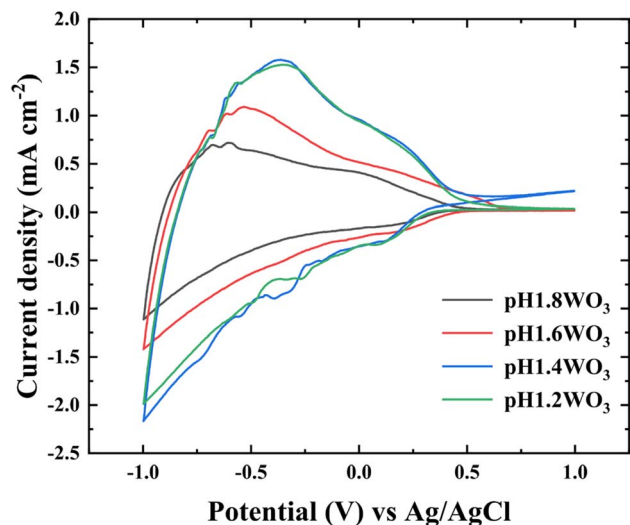
Fig. 5 CV curves of the WO$_3$ films prepared at various pH baths. CV curve plotted from −1.0 to +1.0 V at a sweep rate of 50 mV s^{-1} in the 1.0 M LiClO$_4$ + PC electrolyte.

Table 1 Summary of the diffusion coefficients for WO$_3$ thin films prepared using different pH baths^a

Index	i_c (mA cm^{-2})	i_a (mA cm^{-2})	D_c (cm s^{-1})	D_a (cm s^{-1})
pH1.8WO$_3$	1.112	0.719	3.342×10^{-13}	1.396×10^{-12}
pH1.6WO$_3$	1.419	1.091	5.441×10^{-13}	3.221×10^{-12}
pH1.4WO$_3$	2.116	1.578	1.268×10^{-12}	6.728×10^{-12}
pH1.2WO$_3$	1.988	1.526	1.068×10^{-12}	6.299×10^{-12}

^{a} i_a and D_a represent the anodic peak current density and anodic diffusion coefficient.

One of the most important factors is coloration efficiency (CE), which is the rate of inserting charge (Q_{in}) into the film and optical density (ΔOD). CE was calculated from spectroelectrochemical parameters using the following equation.

$$\text{CE} = \frac{\Delta\text{OD}}{Q_{in}} = \frac{\log(T_b/T_c)}{q/A} \left[\text{cm}^2 \text{ C}^{-1}\right] \qquad (3)$$

where Q_{in} is the charge density during coloration and T_b and T_c are the transmittance at bleaching and coloration states, respectively. Interestingly, the obtained CE results presented different trends from the above results (Fig. 7), and the order of CE in the WO$_3$ films is as follows: 1.4-WO$_3$ (61.92 cm^2 C^{-1}) > 1.8-WO$_3$ (53.41 cm^2 C^{-1}) > 1.2-WO$_3$ (51.98 cm^2 C^{-1}) > 1.6-WO$_3$ (51.72 cm^2 C^{-1}). The highest CE of pH1.4WO$_3$ is because it has a large ERSA and small grain size with a short diffusion length for ions, which could provide fast ion diffusion in a large area. Consequently, rapid ion intercalation/deintercalation reactions can be accelerated to enhance transmittance modulation. Although the pH1.2WO$_3$ had a larger ERSA and smaller grain size than the pH1.4WO$_3$, it did not show better performance. This might be because the densified inside could reduce the accessibility of Li-electrolyte, and higher interfacial resistance disturbs ion hopping.[37,40–43] These drawbacks offset its good
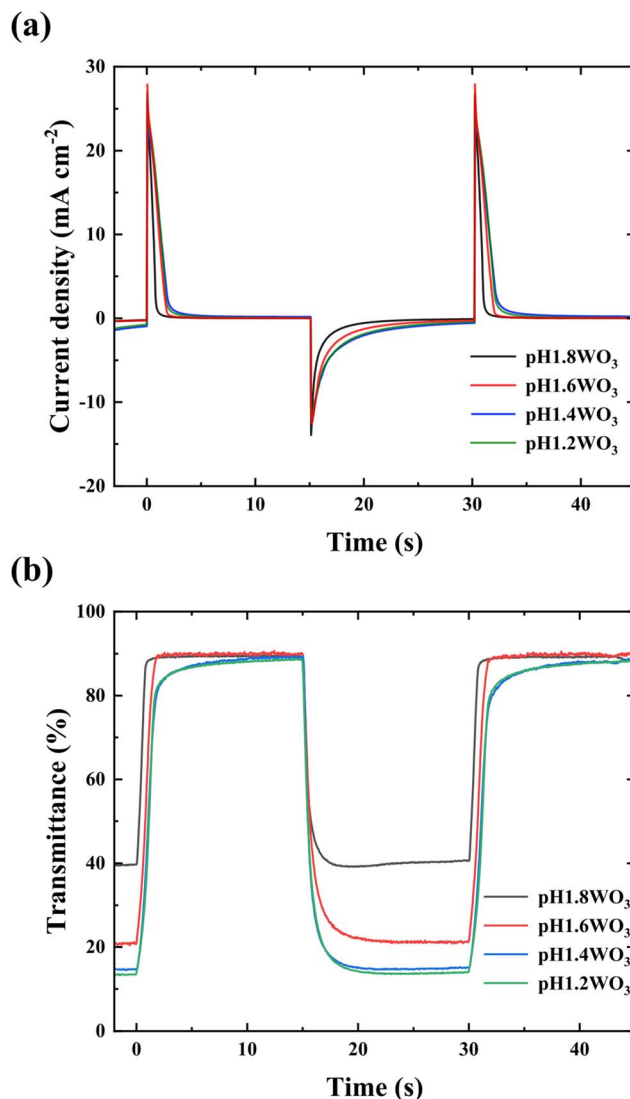

Fig. 6 (a) CA curve for WO$_3$ films, potential range −1.0 to +1.0 V (15 s) in LiClO$_4$ + PC electrolyte; (b) electrochromic response recorded at 650 nm wavelength during chronoamperometry.

structural properties, showing a relatively lower CE value. However, pH1.8WO$_3$ has the largest grain size, longest diffusion length, and the narrowest ERSA in the series of WO$_3$ films, showing higher CE than pH1.2WO$_3$. This unexpected result could be attributed to its small reactive area and thin thickness, which decrease insertion charge density (Q_{in}) and, in turn, increases CE.

Based on the results, an amorphous nanostructure formed by varying nucleation density with electrolyte pH resulted in an effective intercalation/deintercalation reaction with higher CE and rapid switching. In addition, not only tuning surface and inside structure but modifying film thickness would also further improve electrochromic properties. Although pH1.2WO$_3$ had a relatively thicker film, which could not fully utilize its thickness, *i.e.* large storage volume. Therefore, an investigation of films thickness effects and utilization under optimized pH conditions could lead to further improved

Table 2 Electrochromic properties of WO_3 thin films in 1.0 M $LiClO_4$ + PC electrolyte at 650 nm wavelength[a]

Index	T_c (%)	T_b (%)	ΔT (%)	t_c (s)	t_b (s)	Q_c (mC cm^{-2})	Q_b (mC cm^{-2})	Reversibility (%)
pH1.8WO$_3$	39.17	89.65	50.48	1.31	0.80	13.99	13.74	98.21
pH1.6WO$_3$	20.73	90.66	69.93	1.99	1.48	20.97	20.80	99.19
pH1.4WO$_3$	14.62	89.45	74.83	1.56	2.06	33.36	33.24	99.64
pH1.2WO$_3$	13.53	88.72	75.19	1.76	1.96	31.25	30.83	98.66

[a] ΔT = transmittance modulation ($\Delta T = T_b - T_c$), reversibility = $(Q_b/Q_c) \times 100$.
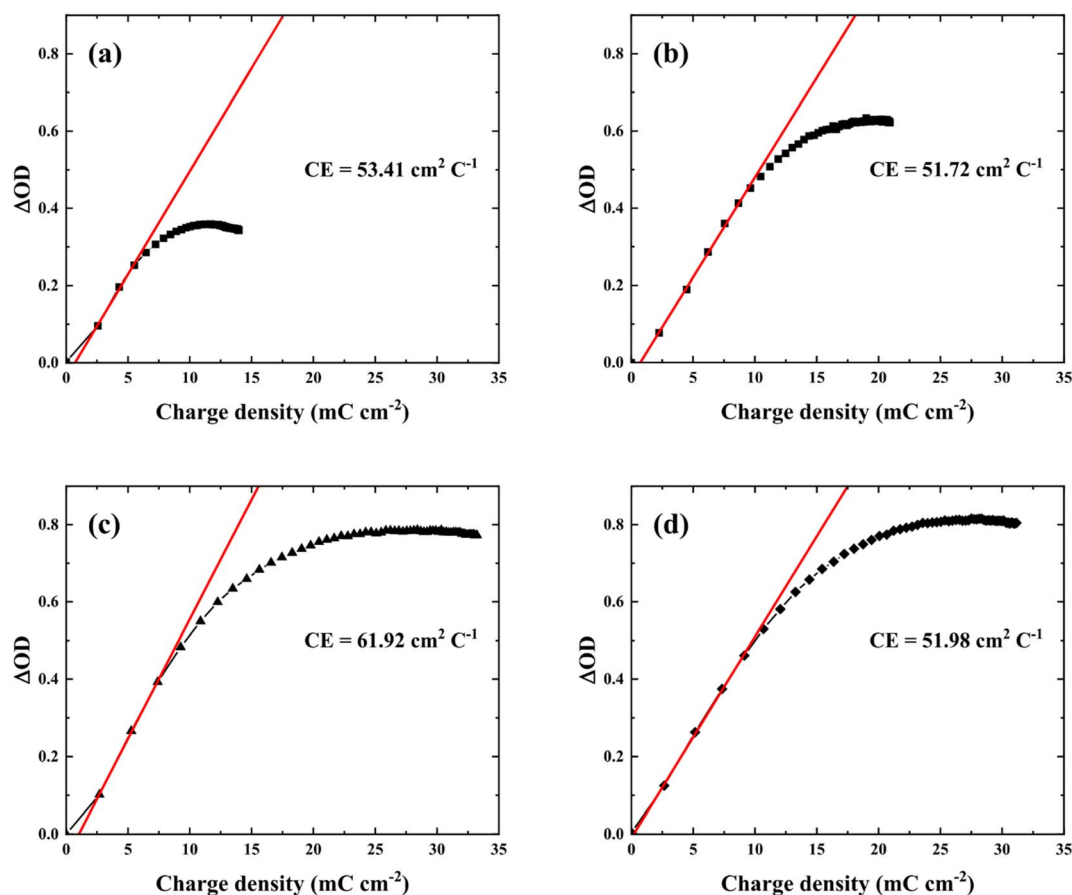
Fig. 7 Optical density *versus* charge density of the WO_3 films prepared at various electrolytes pH, (a) pH 1.8, (b) pH 1.6, (c) pH 1.4, and (d) pH 1.2.

Table 3 Comparison of the electrochromic properties of WO_3 films deposited using different coating techniques

No.	Method	Morphology	Electrolyte	Transmittance modulation (%)	Switching speed (s) t_c	t_b	Coloration efficiency (cm^2 C^{-1})	Ref.
1	Electrodeposition (pH1.4WO$_3$)	Nanoparticle	1 M LiClO$_4$/PC	74.8 (λ = 650 nm)	1.56	2.06	61.9	This study
2	Spin coating	Nanoparticle	1 M LiClO$_4$/PC	54.8 (λ = 633 nm)	11.7	14.6	35.9	11
3	Spin coating	Smooth surface	1 M PEG : LiI	40.0 (λ = 633 nm)	31.7	9.6	34.8	34
4	Electrodeposition	Uniform particle	0.5 M H$_2$SO$_4$	36.7 (λ = 633 nm)	5.3	5.1	62.4	44
5	Electrodeposition	Smooth surface	0.1 M HNO$_3$	68.4 (λ = 632 nm)	3.0	1.0	41.3	27
6	Hydrothermal	Coral-like	1 M LiClO$_4$/PC	78.1 (λ = 630 nm)	5.0	6.0	56.5	45
7	Hydrothermal	Nanobricks	0.5 M LiClO$_4$/PC	28.0 (λ = 630 nm)	9.7	6.9	39.3	23

electrochromic performance, and providing information of correlation between each parameter.

Furthermore, when compared to other electrochromic devices recently reported (Table 3), the pH1.4WO$_3$ showed more improved switching speed and transmittance modulation with comparable CE.[11,23,27,34,44,45]

Conclusions

A series of nanostructured amorphous WO$_3$ films were electrodeposited in a pH-controlled electrolyte. Nucleation density could be controlled with variations in pH, affecting structural differences. The FE-SEM analysis showed that a lower electrolyte pH induces a small grain size; large ERSA and shorter diffusion length promote enhanced electrochromic performance. However, excessively small grain size with fast nucleation causes densified structure, which negatively affects ion diffusion with intercalation/deintercalation. Hence, the appropriate grain size and density of the pH1.4WO$_3$ showed superior electrochromic performance, including higher CE (61.92 cm^2 C^{-1}) and transmittance modulation (74.83%) with quick switching. These results will provide explicit experimental evidence for the rational design of efficient coloration film materials by tuning the nanostructure to improve ion intercalation/deintercalation.

Conflicts of interest

There are no conflicts to declare.

Acknowledgements

References

1 M. A. J. Q. Franco, P. Pawar and X. Wu, *Energy Build.*, 2021, **231**, 110561.

2 I. Sorar, İ. Bayrak Pehlivan, J. Bohlin, C. G. Granqvist and G. A. Niklasson, *Sol. Energy Mater. Sol. Cells*, 2020, **218**, 110767.

3 Y. Yao, Q. Zhao, W. Wei, Z. Chen, Y. Zhu, P. Zhang, Z. Zhang and Y. Gao, *Nano Energy*, 2020, **68**, 104350.

4 M. Brzezicki, *Sustainability*, 2021, **13**, 9604.

5 C. Y. Ng, K. Abdul Razak and Z. Lockman, *Thin Solid Films*, 2015, **595**, 73–78.

6 D. Ma, G. Shi, H. Wang, Q. Zhang and Y. Li, *J. Mater. Chem. A*, 2013, **1**, 684–691.

7 A. Karuppasamy, *Appl. Surf. Sci.*, 2013, **282**, 77–83.

8 L. Ottaviano, A. Pennisi, F. Simone and A. M. Salvi, *Opt. Mater.*, 2004, **27**, 307–313.

9 S. Pereira, A. Gonçalves, N. Correia, J. Pinto, L. Pereira, R. Martins and E. Fortunato, *Sol. Energy Mater. Sol. Cells*, 2014, **120**, 109–115.

10 X. H. Xia, J. P. Tu, J. Zhang, J. Y. Xiang, X. L. Wang and X. B. Zhao, *Sol. Energy Mater. Sol. Cells*, 2010, **94**, 386–389.

11 B.-R. Koo, K.-H. Kim and H.-J. Ahn, *Appl. Surf. Sci.*, 2018, **453**, 238–244.

12 I. Sorar, E. Pehlivan, G. A. Niklasson and C. G. Granqvist, *Sol. Energy Mater. Sol. Cells*, 2013, **115**, 172–180.

13 R. Romero, E. A. Dalchiele, F. Martín, D. Leinen and J. R. Ramos-Barrado, *Sol. Energy Mater. Sol. Cells*, 2009, **93**, 222–229.

14 K. N. Kumar, G. Nithya, H. Shaik, B. Hemanth, M. Chethana, K. Kishore, V. Madhavi, R. I. Jafri, S. A. Sattar, J. Gupta and G. V. A. Reddy, *Phys. B*, 2022, **640**, 413932.

15 K. N. Kumar, H. Shaik, J. Gupta, S. A. Sattar, R. I. Jafri, A. Pawar, V. Madhavi, G. V. A. Reddy and G. Nithya, *Mater. Chem. Phys.*, 2022, **278**, 125706.

16 H. Yu, J. Guo, C. Wang, J. Zhang, J. Liu, G. Dong, X. Zhong and X. Diao, *Electrochim. Acta*, 2020, **332**, 135504.

17 Y.-C. Nah, A. Ghicov, D. Kim and P. Schmuki, *Electrochem. Commun.*, 2008, **10**, 1777–1780.

18 V. Madhavi, P. Kondaiah, O. M. Hussain and S. Uthanna, *Phys. B*, 2014, **454**, 141–147.

19 S.-H. Lee, H. M. Cheong, J.-G. Zhang, A. Mascarenhas, D. K. Benson and S. K. Deb, *Appl. Phys. Lett.*, 1999, **74**, 242–244.

20 M. M. El-Nahass, M. M. Saadeldin, H. A. M. Ali and M. Zaghllol, *Mater. Sci. Semicond. Process.*, 2015, **29**, 201–205.

21 S. Cong, Y. Y. Tian, Q. W. Li, Z. G. Zhao and F. X. Geng, *Adv. Mater.*, 2014, **26**, 4260–4267.

22 P. Yang, P. Sun, Z. Chai, L. Huang, X. Cai, S. Tan, J. Song and W. Mai, *Angew. Chem., Int. Ed.*, 2014, **126**, 12129–12133.

23 V. V. Kondalkar, R. R. Kharade, S. S. Mali, R. M. Mane, P. B. Patil, P. S. Patil, S. Choudhury and P. N. Bhosale, *Superlattices Microstruct.*, 2014, **73**, 290–295.

24 J. M. Ortega, A. I. Martínez, D. R. Acosta and C. R. Magaña, *Sol. Energy Mater. Sol. Cells*, 2006, **90**, 2471–2479.

25 K. J. Patel, C. J. Panchal, V. A. Kheraj and M. S. Desai, *Mater. Chem. Phys.*, 2009, **114**, 475–478.

26 C. Fàbrega, S. Murcia-López, D. Monllor-Satoca, J. D. Prades, M. D. Hernández-Alonso, G. Penelas, J. R. Morante and T. Andreu, *Appl. Catal., B*, 2016, **189**, 133–140.

27 Y.-T. Park and K.-T. Lee, *Opt. Mater.*, 2021, **121**, 111577.

28 J. B. Thorat, S. V. Mohite, A. A. Bagade, T. J. Shinde, V. J. Fulari, K. Y. Rajpure and N. S. Shinde, *Mater. Sci. Semicond. Process.*, 2018, **79**, 119–126.

29 J.-m. Li, C. Cai, L.-x. Song, J.-f. Li, Z. Zhang, M.-z. Xue and Y.-g. Liu, *Trans. Nonferrous Met. Soc. China*, 2013, **23**, 2300–2306.

30 Y. Wang, Z. Meng, H. Chen, T. Li, D. Zheng, Q. Xu, H. Wang, X. Y. Liu and W. Guo, *J. Mater. Chem. C*, 2019, **7**, 1966–1973.

31 K. Thummavichai, L. Trimby, N. Wang, C. D. Wright, Y. Xia and Y. Zhu, *J. Phys. Chem. C*, 2017, **121**, 20498–20506.

32 Q. Huang, H. Deligianni and L. T. Romankiw, *J. Electrochem. Soc.*, 2006, **153**, 332–336.

33 V. S. Kumbhar, J. Lee, Y. Choi, H. Lee, M. Ryuichi, M. Nakayama, W. Lee, H. Oh and K. Lee, *Thin Solid Films*, 2020, **709**, 138214.

34 B. Wen-Cheun Au, K.-Y. Chan and D. Knipp, *Opt. Mater.*, 2019, **94**, 387–392.

35 Z.-j. Xia, H.-l. Wang, Y.-f. Su, P. Tang, M.-j. Dai, H.-j. Lin, Z.-g. Zhang and Q. Shi, *Coatings*, 2020, **10**, 577.

36 H. Chen, N. Xu, S. Deng, J. Zhou, Z. Li, H. Ren, J. Chen and J. She, *J. Appl. Phys.*, 2007, **101**, 114303.

37 S. Wu, B. Yu, Z. Wu, S. Fang, B. Shi and J. Yang, *RSC Adv.*, 2018, **8**, 8544–8551.

38 N. Naseri, R. Azimirad, O. Akhavan and A. Z. Moshfegh, *Thin Solid Films*, 2010, **518**, 2250–2257.

39 L. Shen, G. Luo, J. Zheng and C. Xu, *Electrochim. Acta*, 2018, **278**, 263–270.

40 L. Yang, X. Huang, C. Zou, X. Tao, L. Liu, K. Luo, P. Zeng, Q. Dai, Y. Li, L. Yi, Z. Luo and X. Wang, *Ceram. Int.*, 2021, **47**, 18196–18204.

41 M. Mirzaeian and P. J. Hall, *Electrochim. Acta*, 2009, **54**, 7444–7451.

42 G. Yu, Y. Wang, K. Li, D. Chen, L. Qin, H. Xu, J. Chen, W. Zhang, P. Zhang and Z. Sun, *Sustainable Energy Fuels*, 2021, **5**, 1211–1221.

43 M. Mirzaeian, Q. Abbas, A. Ogwu, P. Hall, M. Goldin, M. Mirzaeian and H. F. Jirandehi, *Int. J. Hydrogen Energy*, 2017, **42**, 25565–25587.

44 H. Najafi-Ashtiani, A. Bahari and S. Ghasemi, *J. Electroanal. Chem.*, 2016, **774**, 14–21.

45 J. Pan, Y. Wang, R. Zheng, M. Wang, Z. Wan, C. Jia, X. Weng, J. Xie and L. Deng, *J. Mater. Chem. A*, 2019, **7**, 13956–13967.